



DEPARTMENT OF PHYSICS AND ASTRONOMY
AARHUS UNIVERSITY

PROGRESS REPORT
PART A QUALIFYING EXAM

MONTE CARLO WAVE PACKET APPROACH TO DISSOCIATIVE DOUBLE
IONIZATION OF H_2 INTERACTING WITH INTENSE LASER PULSES

Author:
Qingli Jing

Supervisor:
Lars Bojer Madsen

December 19, 2016

Preface

This progress report displays part of the work done during part A of my Ph.D. studies at Department of Physics and Astronomy, Aarhus University.

My project is to apply the Monte Carlo wave packet (MCWP) approach to simulate the process of dissociative double ionization of small diatomic molecules interacting with ultrashort and ultrastrong laser pulses. In this report, the nuclear kinetic energy release (KER) spectra after double ionization of H_2 exposed to intense femtosecond laser pulses at near-infrared (near-IR) and mid-infrared (mid-IR) wavelengths are calculated using the MCWP method. The main simulation results we have obtained are presented in Chapter 3, and several of them are taken from a recent paper accepted by Physical Review A [1]. An extension of the MCWP approach to involve the process of autoionization as a result of the excitation of one or more doubly-excited states is now in progress.

As part of my PhD program, a study in MADRID for several weeks next year is planed.

Notation

Atomic units $4\pi\epsilon_0 = \hbar = m_e = e = 1$ are used throughout this report unless stated otherwise.

Acknowledgements

I would like to thank my supervisor Lars Bojer Madsen for his excellent guidance throughout my studies: I always benefit a lot from discussing with him. I would like to thank Lun Yue for helping to develop the simulation codes and for helpful suggestions. I would like to thank Chuan Yu and Peng Xu for proofreading part of this report.

Contents

Preface	i
1 Introduction	1
2 Monte Carlo wave packet approach	3
2.1 TDSE and the molecular Hamiltonian	3
2.2 Ionization as a dissipative process	8
2.3 MCWP approach to dissociative double ionization of H_2	10
2.3.1 Calculation strategy	11
2.3.2 Calculation input	14
3 Dissociative double ionization of H_2 exposed to intense laser pulses	15
3.1 Simulation results for laser pulses of 40 fs at 800 nm	15
3.2 Nuclear KER spectra for single laser pulses	19
3.3 Nuclear KER spectra in a pump-probe scheme	22

4 Dissociative double ionization of H₂ exposed to intense laser pulses under the influence of a doubly-excited state	23
5 Summary and Outlook	25

1 Introduction

Laser physics has been one of the most popular research fields since T. H. Maiman invented the first Ruby laser in 1960 [2]. Owing to a wide variety of potential applications [3], the topic of laser-matter interaction has attracted great research interest over the decades. Recent advances in femtosecond laser technology and attosecond science have opened the possibility of observing and controlling nuclear or electron dynamics in atoms [4], molecules [5], and solids [6]. Femtosecond laser pulses are used to probe and image nuclear dynamics, as the typical timescale of nuclear dynamics is 10-100 femtoseconds (10^{-15} s). The motion of electrons, however, is much faster, which is in a timescale from a few femtoseconds to several hundred attoseconds (10^{-18} s). Thus, to monitor electron dynamics, one needs to resort to even shorter attosecond laser pulses.

To achieve the ambitious goal of controlling chemical reactions, it is of first priority to produce high-quality femtosecond laser pulses. By first introducing mode-locking saturable absorbers [7] into laser cavities and then using compression techniques external to the cavities [8], the pulse durations are reduced to a few femtoseconds, along with the improvement of the average powers, pulse energies and pulse repetition rates. The carrier-envelope phase (CEP) in successive pulses generated by mode-locked lasers, however, is not constant because of dispersion in the cavity. Actually, ultrafast dynamics induced by femtosecond laser pulses may depend significantly on the oscillatory electromagnetic fields, thus knowledge of the CEPs of the applied laser pulses is necessary. This implies that carrier-envelope stabilization of femtosecond lasers is required. For example, through using a self-referencing technique [9], stabilization of the carrier phase with respect to the pulse envelope of ultrashort pulses is achieved.

Advances in femtosecond laser technology have accelerated to produce attosecond laser pulses. The generation of a train of phase-locked attosecond pulses from high harmonic generation (HHG) by focusing a femtosecond laser pulse in a gas jet can be dated back to 2001 [10]. Isolated attosecond pulses, however, have greater potential in the investigation of ultrafast electronic processes. To obtain isolated attosecond pulses, one can either put bandpass filters in front of an attosecond pulse train (APT) [11], or introduce the polarization gating [12] or temporal gating [13] technique into the APT setup. Recent progress in attosecond science has witnessed the generation of a single-cycle isolated attosecond laser pulse [14], which better resolves the ultrafast electron dynamics in atoms and molecules by taking advantages of its short pulse duration.

The availability of the above mentioned new light sources helps to obtain increased knowl-

edge of quantum dynamics of quantum systems. Now it is experimentally accessible to produce femtosecond and attosecond pulses with a peak intensity of 10^{14} W/cm² [15], which are sufficient to rival the Coulomb interaction and hence kick out one or more electrons. For the case of molecules, ionization is often accompanied with dissociation of the nuclei due to electron-nuclei correlation, which is referred as dissociative ionization [16]. Experimentally, one can apply several image techniques to measure separately or in coincidence the kinetic energy release (KER) spectra of the nuclear fragments and the momentum spectra of the photoelectrons. For example, cold target recoil-ion momentum spectroscopy (COLTRIMS) [17] and velocity mapping [18] are two popular image techniques for imaging the momentum and velocity distributions of the charged fragments.

Pump-probe techniques have been widely applied to retrieve the ultrafast dynamics in atoms and molecules for decades. In general, the pump pulse induces the dynamics and the probe pulse snapshots the dynamics at different instants. By scanning the delay between the pump and probe pulses, a movie recording the dynamics is obtained. For example, the reconstruction of attosecond beating by interference of two-photon transition (RABBIT) [19] technique and the streaking camera [20] are developed to obtain the attosecond photoionization time delays. Both the techniques use a weak femtosecond laser pulse as the probe, and in terms of the pump, the former makes use of an APT and the latter an isolated attosecond pulse. The high-energy photons of attosecond pulses, which are usually in the XUV region, can approach or surpass the ionization potential through one-photon absorption. The delayed weak femtosecond laser pulse can either kick out the excited electrons or streak the photoelectrons. Thus, the dynamics induced by the pump pulse is encoded in the delay-dependent photoelectron momentum distributions. By using this pump-probe setting, apart from the process of photoionization, information of autoionization from doubly-excited states in atoms and molecules can also be obtained [21]. In addition, the recent availability of the mid-IR laser sources has promoted the study of the rescattering process of photoelectrons, as the electrons can gain more kinetic energy when returning to the cations. For example, the mid-IR laser pulses have been applied to image molecular structures by light-induced electron diffraction (LIED) and to greatly increase the photon energies of HHG [22].

In parallel to the advances in experimental techniques, several theoretical methods [23, 24, 25], dedicating to solving the time-dependent Schrödinger equation (TDSE), have been developed and proven to work very well in describing a range of phenomena associated with laser-molecule interaction. For example, the multi-configurational time dependent Hartree–Fock method (MCTDHF) [23] is capable of exploring correlated electronic dynamics in small molecules even beyond the Born-Oppenheimer approximation; the time-dependent Feshbach close coupling (TDFCC) [24] method has been widely used to describe ionization processes even in the presence of autoionizing states by using the close-coupling expansion method, in which the total wave function is expanded in the basis of eigenstates of the field-free total Hamiltonian; and the Monte Carlo wave packet (MCWP) approach [26], which is applied in this report, can greatly simplify the problem of solving TDSE as the electronic degrees of freedom are treated within an effective description. By applying

the MCWP approach, information of the nuclear part, e.g., the nuclear KER spectra, can be obtained more easily. For example, as we will show in Chapter 3, the MCWP approach is capable of simulating interaction of small molecules with mid-IR laser pulses with durations of several hundreds of femtoseconds, which is computationally difficult for other methods. Though it is impossible to describe the motion of photoelectrons quantum mechanically by using the MCWP method, a classical description of the emitted photoelectrons within strong-field approximation can, in principle, offer some insights.

This report centers around applying the MCWP approach to simulate dissociative double ionization of small molecules. Chapter 2 shows in detail how to get the molecular Hamiltonian and how to apply the MCWP approach to simulate dissociative double ionization of H_2 exposed to intense laser pulses. In Chapter 3, we present and discuss the results for H_2 interacting with laser pulses under several different durations, peak intensities, and central wavelengths, some of which are taken from our paper recently accepted by Physical Review A. In Chapter 4, we extend our approach to include the influence of a doubly-excited state as well as the process of autoionization on the nuclear KER spectra. New features in the nuclear KER spectra are discussed in particular. Chapter 5 presents the conclusion and outlook of this report.

We hope our new findings in the calculated nuclear KER spectra, with and without the influence of doubly-excited states, can stimulate experimental study of the interaction between molecules and IR wavelengths.

2 Monte Carlo wave packet approach

In this chapter, I will present how to apply the MCWP approach to dissociative double ionization of H_2 interacting with intense laser pulses. Our starting point is to illustrate the detailed procedures to obtain the molecular Hamiltonian and the corresponding TDSE.

2.1 TDSE and the molecular Hamiltonian

The evolution of a system interacting with laser light can be described by the TDSE, i.e.,

$$i\partial_t|\Psi(t)\rangle = H(t)|\Psi(t)\rangle = (H_0 + V_I(t))|\Psi(t)\rangle, \quad (2.1)$$

where H_0 is the field-free Hamiltonian and $V_I(t)$ is the laser-matter interaction operator. When the system we are interested is a molecule, the field-free Hamiltonian can be expressed as

$$H_0 = T_N + V_N + V_{eN} + T_e + V_{ee}, \quad (2.2)$$

where T_N is the kinetic energy operator for the nuclei, T_e the kinetic energy for the electrons, V_N the nuclear repulsion, V_{eN} the nuclei-electron interaction, and V_{ee} the electron-

electron interaction. For a molecule with N nuclei and M electrons, the field-free Hamiltonian is

$$H_0 = \sum_{k=1}^N \frac{\vec{p}_{N,k}^2}{2m_{N,k}} + \sum_{k<j} \frac{z_{N,k}z_{N,j}}{|\vec{r}_{N,k} - \vec{r}_{N,j}|} - \sum_{k,j} \frac{z_{N,k}}{|\vec{r}_{N,k} - \vec{r}_{el,j}|} + \sum_{k=1}^M \frac{\vec{p}_{el,k}^2}{2} + \sum_{k<j} \frac{1}{|\vec{r}_{el,k} - \vec{r}_{el,j}|}, \quad (2.3)$$

where $\vec{r}_{N,k}$ ($\vec{r}_{el,k}$) denotes the position of the k th nucleus (electron) in the laboratory fixed coordinate system and $\vec{p}_{N,k} = -i\nabla_{\vec{r}_{N,k}}$ ($\vec{p}_{el,k} = -i\nabla_{\vec{r}_{el,k}}$) refers to the momentum operator of the k th nucleus (electron). The charge and mass of the k th nucleus are denoted by $z_{N,k}$ and $m_{N,k}$, respectively.

It is well-known that the laser-matter interaction term $V_I(t)$ in Eq. (2.1) in the length gauge is

$$V_I(t) = \sum_{k=1}^M \vec{r}_{el,k} \cdot \vec{F}(t) - \sum_{k=1}^N z_{N,k} \vec{r}_{N,k} \cdot \vec{F}(t), \quad (2.4)$$

where $\vec{F}(t)$ is the external laser electric field. It is worth mentioning that the above equation implies the dipole approximation is applied.

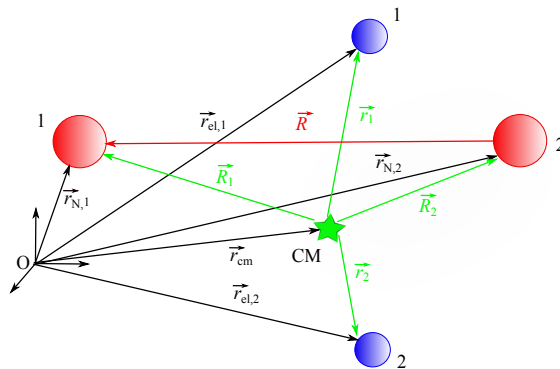


Figure 2.1: Laboratory fixed (black) and relative (green) coordinates for a diatomic molecule. The two nuclei denoted by the red balls are at 1 and 2, with position vectors $\vec{r}_{N,1}$ and $\vec{r}_{N,2}$ with respect to O. Two electrons are drawn as blue balls even though the molecule is assumed to have M electrons. The positions of the electrons with respect to O are denoted by $\vec{r}_{el,1}, \vec{r}_{el,2}, \dots, \vec{r}_{el,M}$. The center of mass is marked CM and its position vector with respect to O is \vec{r}_{cm} . The position vectors of the nuclei (electrons) with respect to CM are denoted by \vec{R}_1 and \vec{R}_2 ($\vec{r}_1, \vec{r}_2, \dots$, and \vec{r}_M). \vec{R} independent of coordinate systems refers to the nuclear separation vector.

When we consider a diatomic molecule ($N = 2$), as the dissociation process of the nuclei is one of the main concerns in this report, it is a better choice to work in the relative coordinate system instead of in the laboratory fixed coordinate system. The relationship between the two coordinate systems is pictured in Fig. 2.1. The two nuclei N_1 and N_2 have masses of $m_{N,1}$ and $m_{N,2}$. They situate in the laboratory (its origin is assumed to be O) with the respective position vectors $\vec{r}_{N,1}$ and $\vec{r}_{N,2}$. Thus, the internuclear position

vector is

$$\vec{R} = \vec{r}_{N,1} - \vec{r}_{N,2}. \quad (2.5)$$

The position vectors of the electrons with respect to O are denoted by $\vec{r}_{\text{el},k}$ ($k = 1, 2, \dots$). We take O_{cm} to be the center of mass of this molecule and its position vector \vec{r}_{cm} with respect to O is

$$\vec{r}_{\text{cm}} = \frac{m_{N,1}\vec{r}_{N,1} + m_{N,2}\vec{r}_{N,2} + \sum_k \vec{r}_{\text{el},k}}{m_{N,1} + m_{N,2} + M}, \quad (2.6)$$

and the position vector of the k th electron with respect to O_{cm} is

$$\vec{r}_k = \vec{r}_{\text{el},k} - \vec{r}_{\text{cm}}. \quad (2.7)$$

Similarly, the position vectors of the two nuclei in the relative coordinate system are \vec{R}_1 and \vec{R}_2 . As O_{cm} is the origin of the center of mass coordinate system, the following equation should be satisfied, i.e.,

$$0 = \frac{m_{N,1}\vec{R}_1 + m_{N,2}\vec{R}_2 + \sum_{k=1}^M \vec{r}_k}{m_{N,1} + m_{N,2} + M}. \quad (2.8)$$

Substituting Eqs. (2.5-2.7) into Eq. (2.3), the field-free Hamiltonian in the laboratory coordinate system is reduced to

$$H_0 = -\frac{\nabla_{\vec{R}}^2}{2\mu} - \sum_{k=1}^M \frac{\nabla_{\vec{r}_k}^2}{2} + \frac{z_{N,1}z_{N,2}}{|\vec{R}|} + \sum_{k < j} \frac{1}{|\vec{r}_k - \vec{r}_j|} - \sum_{k=1}^M \frac{z_{N,1}}{|\vec{r}_k - \vec{R}_1|} - \sum_{k=1}^M \frac{z_{N,2}}{|\vec{r}_k - \vec{R}_2|} + H_{\text{cm}0}, \quad (2.9)$$

where $\mu = m_{N,1}m_{N,2}/(m_{N,1} + m_{N,2})$ is the reduced mass of the nuclei. Combining Eq. (2.8) with the relation of $\vec{R} = \vec{R}_1 - \vec{R}_2$ together, we can express \vec{R}_1 and \vec{R}_2 in the following way,

$$\vec{R}_1 = \frac{m_{N,2}}{m_{N,1} + m_{N,2}} \vec{R} - \frac{1}{m_{N,1} + m_{N,2}} \sum_{k=1}^M \vec{r}_k, \quad (2.10)$$

$$\vec{R}_2 = -\frac{m_{N,1}}{m_{N,1} + m_{N,2}} \vec{R} - \frac{1}{m_{N,1} + m_{N,2}} \sum_{k=1}^M \vec{r}_k. \quad (2.11)$$

In Eq. (2.9), the field-free center of mass Hamiltonian takes the form

$$H_{\text{cm}0} = -\frac{\nabla_{\vec{r}_{\text{cm}}}^2}{2(m_{N,1} + m_{N,2} + M)}. \quad (2.12)$$

In a similar way, we can deduce the laser-matter interaction $V_1(t)$ in the relative coordinate system, i.e.,

$$V_1(t) = \sum_{k=1}^M \vec{r}_k \cdot \vec{F}(t) - \sum_{k=1}^2 z_{N,k} \vec{R}_k \cdot \vec{F}(t) + (M - z_{N,1} - z_{N,2}) \vec{r}_{\text{cm}} \cdot \vec{F}(t). \quad (2.13)$$

From the above analysis, the total Hamiltonian can be rewritten as

$$H(t) = H_{\text{internal}} + H_{\text{cm}}, \quad (2.14)$$

where

$$\begin{aligned}
H_{\text{internal}} = & -\frac{\nabla_{\vec{R}}^2}{2\mu} - \sum_{k=1}^M \frac{\nabla_{\vec{r}_k}^2}{2} + \frac{z_{N,1}z_{N,2}}{|\vec{R}|} + \sum_{k<j} \frac{1}{|\vec{r}_k - \vec{r}_j|} - \sum_{k=1}^M \frac{z_{N,1}}{|\vec{r}_k - \vec{R}_1|} \\
& - \sum_{k=1}^M \frac{z_{N,2}}{|\vec{r}_k - \vec{R}_2|} + \sum_{k=1}^M \vec{r}_k \cdot \vec{F}(t) - \sum_{k=1}^2 z_{N,k} \vec{R}_k \cdot \vec{F}(t), \tag{2.15}
\end{aligned}$$

and

$$H_{\text{cm}} = -\frac{\nabla_{\vec{r}_{\text{cm}}}^2}{2(m_{N,1} + m_{N,2} + M)} + (M - z_{N,1} - z_{N,2}) \vec{r}_{\text{cm}} \cdot \vec{F}(t). \tag{2.16}$$

We can see from the above two equations, the motion of the center of mass is not coupled to any of the internal coordinates. The last term in Eq. (2.15) responsible for the interaction between the nuclei and the applied laser pulse would vanish for the case of homonuclear diatomic molecules. As a result, the total state of the molecule can be express as a product state, i.e.,

$$|\Psi_{\text{total}}\rangle = |\Psi_{\text{internal}}\rangle \otimes |\Psi_{\text{cm}}\rangle. \tag{2.17}$$

The center of mass Hamiltonian describes a charged particle with charge $M - z_{N,1} - z_{N,2}$ and with mass $m_{N,1} + m_{N,2} + M$ moving in an external field $\vec{F}(t)$. The eigenstates of this charged particle are in the form of Volkov waves. For a neutral molecule, because of zero charge of the center of mass, it would move freely without any interaction with the external field. For the case of a charged center of mass, as it can not absorb energy from the radiation field, thus the kinetic energy of the center of mass does not change during the interaction with the external field. This means that we can safely neglect $|\Psi_{\text{cm}}\rangle$ in Eq. (2.17) and we only need to solve the TDSE of the internal system. In the following part of this report, the operators and states are described in this internal system.

In this report, we are interested in obtaining knowledge of the dynamics of H_2 exposed to intense laser pulses. Thus, the Hamiltonian we are dealing within length gauge now reads

$$\begin{aligned}
H(t) = & -\frac{\nabla_{\vec{R}}^2}{2\mu} - \frac{\nabla_{\vec{r}_1}^2}{2} - \frac{\nabla_{\vec{r}_2}^2}{2} + \frac{1}{|\vec{R}|} + \frac{1}{|\vec{r}_1 - \vec{r}_2|} \\
& - \frac{1}{|\vec{r}_1 - \vec{R}_1|} - \frac{1}{|\vec{r}_2 - \vec{R}_1|} - \frac{1}{|\vec{r}_1 - \vec{R}_2|} - \frac{1}{|\vec{r}_2 - \vec{R}_2|} \\
& + \vec{r}_1 \cdot \vec{F}(t) + \vec{r}_2 \cdot \vec{F}(t). \tag{2.18}
\end{aligned}$$

Until now, even though we can easily obtain the Hamiltonian of H_2 , solving its corresponding TDSE remains a tricky task, because it is a four-body problem owning many degrees of freedoms. In order to make this problem solvable, some approximations should be made. One of them is the Born-Oppenheimer approximation. Because of the small ratio of the electronic mass to the nuclear mass, and since the period of a motion is governed by the Heisenberg uncertainty principle ($\Delta t \Delta E \geq \hbar/2$), the nuclear periods are much longer than the electronic periods. Thus the electronic and nuclear motions can be essentially treated independently. The Born-Oppenheimer approximation makes use of this feature and the

electronic states are determined at each value of the internuclear separation by treating the nuclei as fixed. As a result, the Hamiltonian in Eq. (2.18) can now be rearranged as

$$H(t) = T_N(\vec{R}) + H_{\text{el}}(\vec{R}, \vec{r}_1, \vec{r}_2) + V_I(t), \quad (2.19)$$

where

$$T_N = -\frac{\nabla_{\vec{R}}^2}{2\mu} = -\frac{1}{2\mu} \frac{1}{R^2} \left(\frac{\partial}{\partial R} (R^2 \frac{\partial}{\partial R}) - \vec{L}^2 \right), \quad (2.20)$$

$$H_{\text{el}} = -\frac{\nabla_{\vec{r}_1}^2}{2} - \frac{\nabla_{\vec{r}_2}^2}{2} + \frac{1}{|\vec{R}|} + \frac{1}{|\vec{r}_1 - \vec{r}_2|} - \frac{1}{|\vec{r}_1 - \vec{R}_1|} - \frac{1}{|\vec{r}_2 - \vec{R}_1|} - \frac{1}{|\vec{r}_1 - \vec{R}_2|} - \frac{1}{|\vec{r}_2 - \vec{R}_2|}, \quad (2.21)$$

and

$$V_I(t) = \vec{r}_1 \cdot \vec{F}(t) + \vec{r}_2 \cdot \vec{F}(t). \quad (2.22)$$

\vec{L} in Eq. (2.20) is the orbital angular momentum operator and \vec{L}^2 is expressed as

$$\vec{L}^2 = -\left(\frac{1}{\sin \theta} \frac{\partial}{\partial \theta} (\sin \theta) \frac{\partial}{\partial \theta} + \frac{1}{\sin \theta} \frac{\partial^2}{\partial \phi^2} \right), \quad (2.23)$$

where (R, θ, ϕ) is the spherical polar coordinates of \vec{R} . The electronic basis states $|\phi_{R,k}^{\text{el}}\rangle$ can be obtained through solving the electronic time-independent Schrödinger equation with parametric dependence on \vec{R} , i.e.,

$$H_{\text{el}}|\phi_{R,k}^{\text{el}}\rangle = E_{\text{el},k}(\vec{R})|\phi_{R,k}^{\text{el}}\rangle. \quad (2.24)$$

The total wave function for the molecule can be expanded as

$$|\Psi(t)\rangle = \sum_k \int d\vec{R} G_k(\vec{R}, t) |\phi_{R,k}^{\text{el}}\rangle \otimes |\vec{R}\rangle, \quad (2.25)$$

where the expansion coefficients $G_k(\vec{R}, t)$ are wave functions representing the nuclear motion when the electronic system is in the state $|\phi_{R,k}^{\text{el}}\rangle$. By inserting Eq. (2.25) into the following TDSE

$$i\partial_t |\Psi(t)\rangle = (T_N(\vec{R}) + H_{\text{el}}(\vec{R}, \vec{r}_1, \vec{r}_2) + V_I(t)) |\Psi(t)\rangle \quad (2.26)$$

and projecting on the electronic basis ket $\langle \phi_{R,j}^{\text{el}} |$, the time evolution of the nuclear wave function $G_j(\vec{R}, t)$ is then obtained, i.e.,

$$\begin{aligned} i\partial_t G_j(\vec{R}, t) &= \left(-\frac{1}{2\mu R^2} \frac{\partial}{\partial R} (R^2 \frac{\partial}{\partial R}) + E_{\text{el},j}(\vec{R}) \right) G_j(\vec{R}, t) \\ &- \frac{1}{2\mu} \sum_k \langle \phi_{R,j}^{\text{el}} | \frac{\partial^2}{\partial R^2} | \phi_{R,k}^{\text{el}} \rangle G_k(\vec{R}, t) \\ &- \frac{1}{\mu} \frac{1}{R} \sum_k \langle \phi_{R,j}^{\text{el}} | \frac{\partial}{\partial R} | \phi_{R,k}^{\text{el}} \rangle G_k(\vec{R}, t) \\ &- \frac{1}{\mu} \sum_k \langle \phi_{R,j}^{\text{el}} | \frac{\partial}{\partial R} | \phi_{R,k}^{\text{el}} \rangle \frac{\partial}{\partial R} G_k(\vec{R}, t) \\ &+ \frac{1}{2\mu R^2} \sum_k \langle \phi_{R,j}^{\text{el}} | \vec{L}^2 | \phi_{R,k}^{\text{el}} \rangle G_k(\vec{R}, t) \\ &+ \sum_k \langle \phi_{R,j}^{\text{el}} | \vec{r}_1 + \vec{r}_2 | \phi_{R,k}^{\text{el}} \rangle \cdot \vec{F}(t) G_k(\vec{R}, t). \end{aligned} \quad (2.27)$$

The Born-Oppenheimer approximation implies that the electronic wave functions vary very lowly with respect to R , θ and ϕ , which means that $|\partial|\phi_{R,k}^{\text{el}}\rangle/\partial R|$ is very small compared with $|\partial G_k/\partial R|$. Thus terms in Eq. (2.27) containing $\partial|\phi_{R,k}^{\text{el}}\rangle/\partial R$ can be neglected. Further assuming the nuclei are rotational-frozen, equation (2.27) is then reduced to

$$\begin{aligned} i\partial_t G_j(\vec{R}, t) &= \left(-\frac{1}{2\mu R^2} \frac{\partial}{\partial R} (R^2 \frac{\partial}{\partial R}) + E_{\text{el},j}(\vec{R})\right) G_j(\vec{R}, t) \\ &+ \sum_k \langle \phi_{R,j}^{\text{el}} | \vec{r}_1 + \vec{r}_2 | \phi_{R,k}^{\text{el}} \rangle \cdot \vec{F}(t) G_k(\vec{R}, t). \end{aligned} \quad (2.28)$$

Actually, solving the above sets of coupled equations exactly remains impossible, as a result of many electronic bound states as well as the unlimited number of continuum electronic states in the system. Fortunately, reducing the number of either the involved electronic states or the dipole coupling channels to a computer-accessible level is sufficient to simulate the mainly interested physical processes.

2.2 Ionization as a dissipative process

Imagine there are virtual electron detectors outside our system. Once the ionization occurs, there would be a collapse of the system state onto a specific charge state because of these virtual detectors. These different charge states actually represents different Hilbert spaces. The interaction of H_2 with the near-IR and mid-IR laser pulses is mainly studied in this report, which means the photon energies are much smaller than the ionization potentials of H_2 and H_2^+ . Thus, it is reasonable to make the following argument: The laser pulse can couple the electronic states within the same Hilbert space directly; the laser pulse can not directly couple the electronic states in different spaces while it can connect the adjacent two Hilbert spaces through an effective quantum jump. The emitted electrons are assumed to be absorbed by the virtual electron detectors, the rescattering of the photoelectrons by the ion in the laser field is not considered at this moment. As a result, the quantum jump here is unidirectional, which means that the system state can only jump to a higher charge state from a lower charge state, and the other jump direction is not allowed. This kind of treatment is also called the Born-Markov approximation.

Based on the above analysis, we can rewrite Eq. (2.28) as

$$\begin{aligned} i\partial_t G_j(\vec{R}, t) &= \left(-\frac{1}{2\mu R^2} \frac{\partial}{\partial R} (R^2 \frac{\partial}{\partial R}) + E_{\text{el},j}(\vec{R})\right) G_j(\vec{R}, t) \\ &+ \sum_{k'} \langle \phi_{R,j}^{\text{el}} | \vec{r}_1 + \vec{r}_2 | \phi_{R,k'}^{\text{el}} \rangle \cdot \vec{F}(t) G_{k'}(\vec{R}, t) - i \frac{\Gamma_j(\vec{R}, t)}{2} G_j(\vec{R}, t), \end{aligned} \quad (2.29)$$

where k' denotes the electronic states in the same Hilbert space with the j th electronic state and the last term in Eq. (2.29) is responsible for the gradually lost of electrons to surroundings. $\vec{r}_1 + \vec{r}_2$ here means the total electronic coordinate, i.e., $\vec{r}_1 + \vec{r}_2$ for H_2 , \vec{r} for H_2^+ , and zero vector for H_2^{++} . If we assume the initial probability of the electrons is 1,

i.e., $\sum_j \int d\vec{R} |G_j(\vec{R}, t)|^2 = 1$, then this probability would be decreasing over time. This is because the probability of the electrons in each electronic state is decreasing with time, as is seen from the following equation,

$$\partial_t |G_j(\vec{R}, t)|^2 = -\Gamma_j(\vec{R}, t) |G_j(\vec{R}, t)|^2, \quad (2.30)$$

which is deduced from Eq. (2.29). It is worth mentioning that $\Gamma_j(\vec{R}, t)$ here refers to the R -dependent instantaneous ionization rate of the j th electronic state. For a small time dt , the drop in the probability is

$$dP = \sum_j \int d\vec{R} \Gamma_j(\vec{R}, t) |G_j(\vec{R}, t)|^2 dt. \quad (2.31)$$

The considered molecular system exposed to intense laser pulses can be treated as an open system which couples to its surroundings (virtual electron detectors) and ionization is interpreted as a dissipative process. In fact, for open systems, we can also reach equation (2.30) through introducing a non-Hermitian term into the system Hamiltonian, i.e.,

$$H(t) = T_N(\vec{R}) + H_{\text{el}}(\vec{R}, \vec{r}_1, \vec{r}_2) + V_1(t) - \frac{i}{2} \sum_k C_k^+ C_k, \quad (2.32)$$

where C_k is the jump operator, which is responsible for the jump between two Hilbert spaces, i.e.,

$$C_k |\phi_{R,k}^{\text{el}}\rangle = \sum_{k''} c_{k''} |\phi_{R,k''}^{\text{el}}\rangle \quad (2.33)$$

where k'' means the electronic states in the Hilbert space of the adjacent higher charge state and the state after the jump is a coherent superposition of the involved electronic states. Thus the jump operator should be in a form

$$C_k = \sum_{k''} \int d\vec{R} c_{k''} |\phi_{R,k''}^{\text{el}}\rangle \langle \phi_{R,k}^{\text{el}}| \otimes |\vec{R}\rangle \langle \vec{R}|. \quad (2.34)$$

Now it is time to deduce the coefficients $c_{k''}$. If we propagate the quantum state $|\Psi(t)\rangle$ for a small time dt using the non-Hermitian Hamiltonian in Eq. (2.32), we can get

$$|\Psi(t+dt)\rangle = \exp(-iHdt) |\Psi(t)\rangle \approx (1 - iHdt) |\Psi(t)\rangle. \quad (2.35)$$

The drop of the norm square of this new state with respect to that of $|\Psi(t)\rangle$ is

$$dP = \langle \Psi(t) | \sum_k C_k^+ C_k dt | \Psi(t) \rangle = \sum_k \int d\vec{R} A_k |G_k(\vec{R}, t)|^2 dt, \quad (2.36)$$

where $A_k = \sum_{k''} |c_{k''}|^2$. Comparing Eq. (2.36) and Eq. (2.31), we get to know $\Gamma_k(\vec{R}, t) = \sum_{k''} |c_{k''}|^2$.

In addition, the molecule is assumed to be rotational frozen, the radial and angular parts of the nuclear wave function can be separated, i.e.,

$$G_j(\vec{R}, t) = \frac{K_j(R, t)}{R} \frac{1}{\sqrt{4\pi}} \delta(\theta - \theta_0) \delta(\phi - \phi_0) \quad (2.37)$$

where $K_j(R, t)$ denotes the radial nuclear wave function and θ_0 and ϕ_0 specify the internuclear orientation. In our calculations, we consider the case where the molecule is aligned with the linear polarization of the external field, i.e., $\theta_0 = 0^\circ$ and $\phi_0 = 0^\circ$, where the latter can be arbitrary because of symmetry. Taking Eq. (2.37) into Eq. (2.29), simplified form of evolution of $K_j(R, t)$ is obtained, i.e.,

$$i\partial_t K_j(R, t) = \left(-\frac{1}{2\mu} \frac{\partial^2}{\partial R^2} + E_{\text{el},j}(R)\right) K_j(R, t) + \sum_{k'} \langle \phi_{R,j}^{\text{el}} | \vec{r}_1 + \vec{r}_2 | \phi_{R,k'}^{\text{el}} \rangle \cdot \vec{F}(t) K_{k'}(R, t) - i \frac{\Gamma_j(R, t)}{2} K_j(R, t). \quad (2.38)$$

The above simplification reduces the position vector \vec{R} to internuclear separation scalar R , thus the more difficult three dimensional problem eventually becomes the much simpler one dimensional problem. We should point it now, in the following part, the nuclear wave function actually means the radial nuclear wave function in Eq. (2.38).

2.3 MCWP approach to dissociative double ionization of H_2

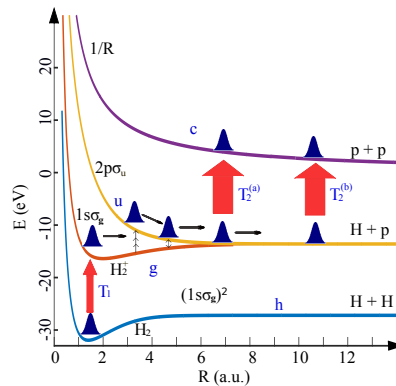


Figure 2.2: Sketch of four field-free Born-Oppenheimer electronic potential energy curves.

It is known that dissipative processes are often handled by solving the master equation of a density matrix. In fact, they can also be simulated by the MCWP approach, which makes use of a stochastic average over different wave functions. For a problem of N_s states, the density matrix has $N_s \times N_s$ entries while a state vector has only N_s entries. Therefore, the computational effort for some problems is reduced in the latter case. In the following, we will take the example of H_2 to illustrate how to apply the MCWP approach to dissociative double ionization.

In Fig. 2.2, four field-free Born-Oppenheimer electronic potential energy curves are sketched. These curves are the $(1s\sigma_g)^2$ ground-state curve in H_2 labeled by h , the $1s\sigma_g$ and $2p\sigma_u$ curves in H_2^+ labeled by g and u , respectively, and the $1/R$ Coulombic curve labeled by c . A particular realization of a quantum trajectory with the MCWP approach

is also shown: At some instant T_1 , the first ionization occurs and the neutral wave packet is promoted to the singly-ionized system where coherent evolution takes place. At some later instant T_2^j ($j = a, b$), the second ionization occurs and then the nuclei undergo Coulomb repulsion. The final energy of the protons depends on the instants T_1, T_2^j .

According to Eq. (2.34), the jump operators responsible for the first and second ionizations in H_2 can be expressed as

$$C_h = \int d\vec{R} \sqrt{\Gamma_h(\vec{R}, t)} (c_g |\phi_{R,g}^{\text{el}}\rangle + c_u |\phi_{R,u}^{\text{el}}\rangle) \langle \phi_{R,h}^{\text{el}} | \otimes |\vec{R}\rangle \langle \vec{R}| \quad (2.39)$$

$$C_g = \int d\vec{R} \sqrt{\Gamma_g(\vec{R}, t)} |\phi_{R,c}^{\text{el}}\rangle \langle \phi_{R,g}^{\text{el}} | \otimes |\vec{R}\rangle \langle \vec{R}| \quad (2.40)$$

$$C_u = \int d\vec{R} \sqrt{\Gamma_u(\vec{R}, t)} |\phi_{R,c}^{\text{el}}\rangle \langle \phi_{R,u}^{\text{el}} | \otimes |\vec{R}\rangle \langle \vec{R}|, \quad (2.41)$$

where $\Gamma_h(\vec{R}, t)$ is the instantaneous ionization rate from the $(1s\sigma_g)^2$ state to the H_2^+ system, and $\Gamma_g(\vec{R}, t)$ ($\Gamma_u(\vec{R}, t)$) corresponds to the ionization rate to H_2^{++} from the $1s\sigma_g$ ($2p\sigma_u$) states in H_2^+ . In the above equations, the expression for c_g and c_u can be found in Ref. [27].

2.3.1 Calculation strategy

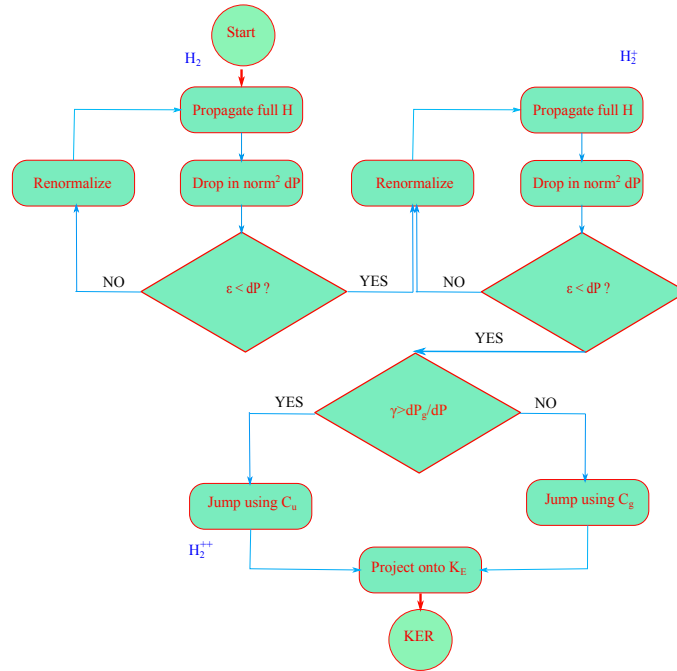


Figure 2.3: Flow diagram of the MCWP approach to dissociative double ionization of H_2 .

A stochastic realization of the MCWP technique is outlined by the flow diagram in Fig. 2.3. The initial nuclear wave function $K_h(R, t_0)$ first evolves in H_2 according to Eq. (2.38). The norm square of the nuclear wave packet is decreasing over time because of the non-Hermitian term in the total Hamiltonian. At each time step, according to Eq. (2.36), the drop in the norm square dP now becomes

$$dP = \int dR \Gamma_h(R, t) |K_h(R, t)|^2 dt. \quad (2.42)$$

Whether the transition from H_2 to H_2^+ occurs or not depends on the comparison of dP with a random number ϵ ($0 \leq \epsilon \leq 1$). If dP is smaller than ϵ , ionization does not occur, and the nuclear wave function is renormalized to prepare for evolution in H_2 to the next time step. The random number ϵ is updated at every time step. The comparison procedure continues until the first jump occurs at some instant T_1 , with dP larger than ϵ . Because of the first jump, the total state in H_2^+ then becomes $C_h|\Psi(T_1)\rangle$,

$$C_h|\Psi(T_1)\rangle = \int dR \sqrt{\Gamma_h(R, T_1)} K_h(R, T_1) (c_g |\phi_{R,g}^{\text{el}}\rangle + c_u |\phi_{R,u}^{\text{el}}\rangle) \otimes |R\rangle. \quad (2.43)$$

We can see from the above equation that the initial nuclear wave functions along the $1s\sigma_g$ and $2p\sigma_u$ curves in H_2^+ are

$$K_g(R, T_1) = \sqrt{\Gamma_h(R, T_1)} c_g K_h(R, T_1), \quad (2.44)$$

and

$$K_u(R, T_1) = \sqrt{\Gamma_h(R, T_1)} c_u K_h(R, T_1). \quad (2.45)$$

To propagate in the H_2^+ system according to Eq. (2.38), the nuclear wave functions also need to be renormalized, i.e., $\int dR |K_g(R, T_1)|^2 + |K_u(R, T_1)|^2 = 1$. The drop in the norm square of the nuclear wave packets in H_2^+ at each time step is

$$dP = \int dR (\Gamma_g(R, t) |K_g(R, t)|^2 + \Gamma_u(R, t) |K_u(R, t)|^2) dt. \quad (2.46)$$

Similarly, if dP is smaller than ϵ , ionization can not occur and the wave functions need to be renormalized. The comparison continues until $dP > \epsilon$ at some instant T_2 , meaning the occurrence of the second jump. The difference in this case is that there are two pathways for the second jump to H_2^{++} , from the $1s\sigma_g$ state and from the $2p\sigma_u$ state, which means that another random number γ ($0 \leq \gamma \leq 1$) should be introduced to decide which pathway to choose. The drop of the nuclear norm square from the $1s\sigma_g$ state in H_2^+ at each time step is

$$dP_g = \int dR \Gamma_g(R, t) |K_g(R, t)|^2 dt. \quad (2.47)$$

If γ is smaller than dP_g/dP , the second jump takes place from the $1s\sigma_g$ state, otherwise, the second jump takes place from the $2p\sigma_u$ state. As a result, the total state can either be $C_g|\Psi(T_2)\rangle$ or be $C_u|\Psi(T_2)\rangle$. Thus the nuclear wave function in H_2^{++} is either

$$K_c(R, T_2) = \sqrt{\Gamma_g(R, T_2)} K_g(R, T_2), \quad (2.48)$$

or

$$K_c(R, T_2) = \sqrt{\Gamma_u(R, T_2)} K_u(R, T_2). \quad (2.49)$$

Once we have in hand the nuclear wave packet in H_2^{++} , it is time to project it on Coulomb waves $K_E(R)$ to get the KER spectrum for protons for the stochastic realization specified by T_1 and T_2 , i.e.,

$$\text{KER}_m(T_1, T_2) = \left| \int K_E(R) K_c(R, T_2) dR \right|^2, \quad (2.50)$$

with $m = g$ or u . In fact, $K_E(R)$ are eigenstates of the Coulomb problems and can be obtained by analytically or numerically solving the following equation

$$\left(-\frac{1}{2\mu} \frac{d^2}{dR^2} + \frac{1}{R} \right) K_E(R) = E K_E(R). \quad (2.51)$$

Equation (2.50) only gives the KER spectrum for one double ionization event occurring at specific T_1 and T_2 . We refer to such a specific realization of jump times and dynamics as a quantum trajectory. The physical nuclear KER spectra of the dissociative double ionization process can be obtained by summing over the KER spectra for many stochastic trajectories.

In the present case of dissociative double ionization, the computational effort can, however, be dramatically reduced through eliminating all the random numbers by applying a completely deterministic approach. To this end, the two jumps which are dressed with probabilities are assumed to take place at every time step. Actually, the probability for each jump is proportional to the drop in the norm square at that jump time. This is reasonable as the larger the drop in the norm square, the more likely it is for a jump to occur. Summing over all the weighted events, the nuclear KER spectrum can be obtained by using the formula below, i.e.,

$$\text{KER}_{\text{tot}} = \sum_{T_1, T_2} P_1 P_{12} \sum_{m=g, u} P(m|\{T_1, T_2\}) \text{KER}_m(T_1, T_2). \quad (2.52)$$

In the above equation,

$$P_1 = -\frac{d(N_h(t))}{dt} \quad (2.53)$$

is the probability density for the first jump with $N_h(t) = \int dR |K_h(R, t)|^2$ representing the integrated norm square of the nuclear wave function of the h state without the first jump;

$$P_{12} = -\frac{d(N_g(t) + N_u(t))}{dt} \quad (2.54)$$

is the conditional probability density for the second jump for a given first jump with $N_g(t) = \int dR |K_g(R, t)|^2$ and $N_u(t) = \int dR |K_u(R, t)|^2$ representing the integrated norm squares of the nuclear wave packets in the g and u states without the second jump, respectively; and

$$P(m|\{T_1, T_2\}) = \frac{\langle \Psi | C_m^+ C_m | \Psi \rangle}{\langle \Psi | C_g^+ C_g + C_u^+ C_u | \Psi \rangle} \quad (2.55)$$

is the conditional probability density from the m (g or u) state for given first and second jump times.

As shown in Fig. 2.2, the initial nuclear wave function is assumed to be ground state of the $(1s\sigma_g)^2$ potential energy curve of H_2 . The applied laser pulse with polarization axis parallel to the molecular axis first kicks out the first electron and then induces nuclear motion in the two potential energy curves in H_2^+ . Meanwhile, there is electronic dipole coupling between the $1s\sigma_g$ and $2p\sigma_u$ states. Finally, the nuclei experience Coulomb repulsion after emitting the second electron. Thus the nuclei pick up energy from two terms, one is the dissociative kinetic energy in the singly-ionized system and the other is the Coulomb repulsion energy in the doubly-ionized system.

2.3.2 Calculation input

Numerically, within each Hilbert space, we solve Eq. (2.38) by applying the split-operator method [28] on the short-time propagator, i.e.,

$$\begin{aligned} U(t + \Delta t, t) &= \exp(-iT_N \frac{\Delta t}{2}) \exp(-iV(R, t + \frac{\Delta t}{2}) \Delta t) \\ &\times \exp(-iT_N \frac{\Delta t}{2}), \end{aligned} \quad (2.56)$$

with the one dimensional $T_N = -\frac{d^2}{2\mu} \frac{d^2}{dR^2}$. Obviously, it is the term $V(R, t)$ that determines how the wave packet evolves in each Hilbert space. In H_2 , only one electronic state is considered in our calculation, therefore,

$$V(R, t) = E_{\text{el,h}}(R) - i \frac{\Gamma_{\text{h}}(R, t)}{2}. \quad (2.57)$$

In the above equation, the instantaneous ionization rate $\Gamma_{\text{h}}(R, t)$ is calculated using the weak-field asymptotic theory in Ref. [29] and the electronic potential energy in Fig. 2.2 is approximated by a Morse potential, i.e.,

$$E_{\text{el,h}}(R) = 0.1819[\exp(-2.01(R - 1.4) - 2.00 \exp(-1.01(R - 1.4)))] - 1.0 \quad (2.58)$$

In H_2^+ system, two electronic states are considered, thus $V(R, t)$ is the 2-by-2 matrix. The four matrix elements are expressed as

$$\begin{aligned} V_{\text{gg}}(R, t) &= E_{\text{el,g}}(R) - \frac{i\Gamma_{\text{g}}(R, t)}{2}, \\ V_{\text{gu}}(R, t) &= \beta D_{\text{gu}}(R) F(t), \\ V_{\text{ug}}(R, t) &= \beta D_{\text{ug}}(R) F(t), \\ V_{\text{uu}}(R, t) &= E_{\text{el,u}}(R) - \frac{i\Gamma_{\text{u}}(R, t)}{2}, \end{aligned} \quad (2.59)$$

where $\beta = 1 + 1/(2m_{\text{p}} + 1)$ with m_{p} the proton mass, $F(t)$ is the laser electric field, and $D_{ij}(R)$ is the electronic dipole moment function between i and j states along the direction,

$\hat{\epsilon}$, of the linear polarization, i.e., $D_{ij}(R) = -\langle \phi_{R,i}^{el} | \vec{r} \cdot \hat{\epsilon} | \phi_{R,j}^{el} \rangle$. We use the explicit expression for D_{gu} , i.e.,

$$D_{\text{gu}}(R) = \frac{R}{2\sqrt{1 - ((1 + R + R^2/3)e^{-R})^2}} - \frac{1}{(2 + 1.4R)}, \quad (2.60)$$

which is given in Ref. [30]. The two channel-resolved instantaneous ionization rates are obtained by interpolating the results published in Ref. [31]. The two electronic potential energies shown in Fig. 2.2 are also approximated by Morse potentials, i.e.,

$$E_{\text{el,g}}(R) = 0.1025[\exp(-1.44(R - 2)) - 2.00 \exp(-0.72(R - 2))] - 0.5, \quad (2.61)$$

$$E_{\text{el,u}}(R) = 0.1025[\exp(-1.44(R - 2)) + 2.22 \exp(-0.72(R - 2))] - 0.5. \quad (2.62)$$

In H_2^{++} , $V(R, t)$ is the Coulomb repulsion between the two protons, i.e.,

$$V(R, t) = \frac{1}{R}. \quad (2.63)$$

We are not interested the evolution of the nuclear wave packet in H_2^{++} . As a result, once the second jump occurs, the nuclear wave function $K_c(R, T_2)$ is projected on Coulomb waves.

The size of our simulation box is 40.96. The time step Δt is 0.1 and the spatial step ΔR is 0.02. The operators $\exp(-iT_N \frac{\Delta t}{2})$ and $\exp(-iV(R, t + \frac{\Delta t}{2})\Delta t)$ are diagonal in the momentum and position representations, respectively, thus a fast-Fourier-transform algorithm is applied in the implementation. To reduce the computational effort further and without reducing the performance of the MCWP approach, all the first jumps are assumed to take place at field extrema and the second jumps at every tenth time step after the first jumps throughout this report.

3 Dissociative double ionization of H_2 exposed to intense laser pulses

In this Chapter, the nuclear KER spectra after dissociative double ionization of H_2 interacting with intense femtosecond laser pulses are presented and analyzed. Throughout this report, all the applied laser pulses have Gaussian envelopes and are linearly polarized with their polarization axes parallel to the molecular axis. In our calculations, the duration of a laser pulse is defined as the full-width-half-maximum (FWHM) of its intensity profile. In the following, two cases are considered: (1) a single pulse is applied; (2) two pulses with a tunable time delay are applied in a pump probe way.

3.1 Simulation results for laser pulses of 40 fs at 800 nm

In this section, we will present the simulation results for H_2 interacting with laser pulses with a duration of 40 fs (15 optical cycles at 800 nm) and with peak intensities ranging

from 4×10^{13} W/cm² to 8×10^{13} W/cm². The case of H₂ interacting with the laser pulse with a peak intensity of 6×10^{13} W/cm² is our starting point. The evolution of the nuclear wave packet $K_h(R, t)$ in H₂ is calculated and its norm square $|K_h(R, t)|^2$ is shown in Fig. 3.1(a). Even though the variation of $|K_h(R, t)|^2$ is not obvious during its propagation, the probability of the nuclear wave packet, i.e., $\int dR |K_h(R, t)|^2$, is gradually decreasing over time [Fig. 3.1(c)], because of the non-Hermitian term in the full Hamiltonian [see Eq. (2.32)]. The decreasing velocity of the probability, which is described in Eq. (2.36), directly depends on the electric field of the applied laser pulse [Fig. 3.1(d)]. This is because the ionization rate $\Gamma_h(R, t)$ is dependent on the instantaneous electric field strength in a natural way: the larger the field strength is, the larger the ionization rate is.

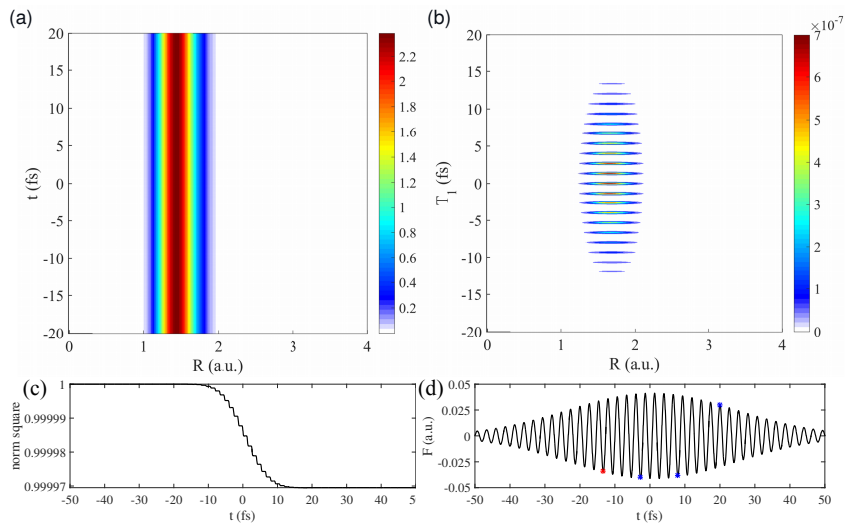


Figure 3.1: (a) Evolution of the norm square of the nuclear wave packet $K_h(R, t)$ along the $(1s\sigma_g)^2$ curve in H₂. (b) The amount of the neutral population entering the $1s\sigma_g$ state in H₂⁺, as a function of the first jump time T_1 . (c) The decreasing behavior of the probability, i.e., $\int dR |K_h(R, t)|^2$, in H₂. (d) The applied laser electric field, i.e., 800 nm, 40 fs and a peak intensity of 6×10^{13} W/cm².

In Fig. 3.1(b), the norm square of the initial wave packet after the first jump and before renormalization, i.e., $c_g \sqrt{\Gamma_h(R, T_1)} K_h(R, T_1)$, for evolution along the $1s\sigma_g$ curve in H₂⁺ is displayed as a function of the first jump time T_1 . In fact, c_g is approximately 1 for the considered peak intensities. Fig. 3.1(b) also shows the amount of the neutral population entering the $1s\sigma_g$ state in H₂⁺. Here we do not present the much smaller population entering the $2p\sigma_u$ state in H₂⁺, since c_u is much smaller than c_g . We can see from Fig. 3.1(b) that the first jump taking place at the field extrema would provide the largest populations entering into the $1s\sigma_g$ state. Thus, our implementation in the deterministic approach that the first jump only occurs at the field extrema is appropriate and reasonable. Apart from that, it is worth mentioning that compared with the nuclear wave packet in H₂, the initial nuclear wave packets in H₂⁺ are slightly shifted to larger internuclear separations, which

results from the R -dependence of the ionization rate $\Gamma_h(R, t)$.

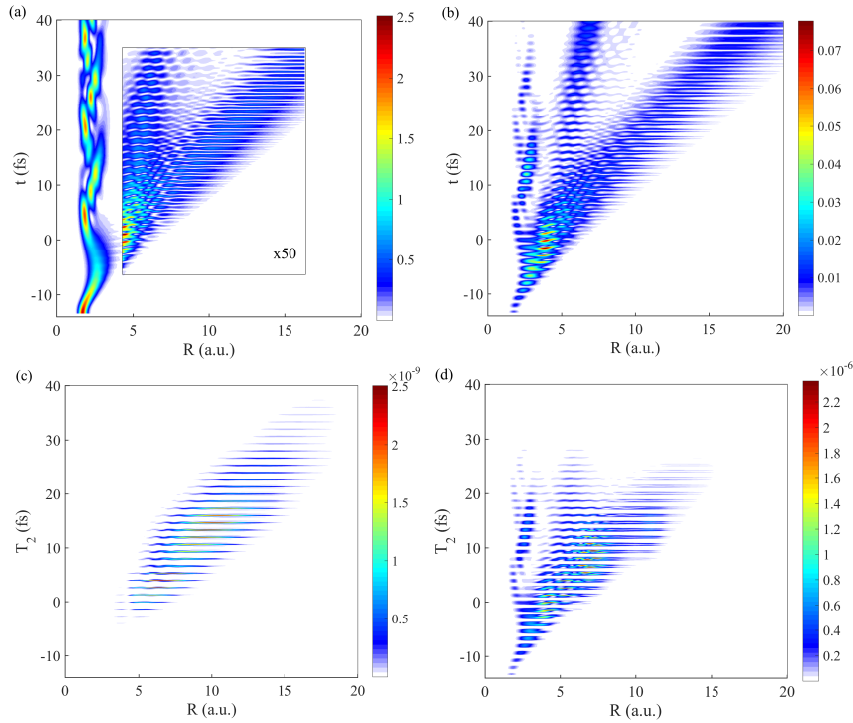


Figure 3.2: Simulation results for H_2^+ at a specific first jump time $T_1 = -13.4$ fs. (a) Evolution of the norm square of the nuclear wave packet $K_g(R, t)$ along the $1s\sigma_g$ curve. The signal in the inset is multiplied by a factor of 50 for better visualization of the weak signal. (b) Evolution of the norm square of the nuclear wave packet $K_u(R, t)$ along the $2p\sigma_u$ curve. (c) The norm square of the nuclear wave packet from the $1s\sigma_g$ state entering the doubly ionized state for different second jump times T_2 , i.e. $\Gamma_g(R, T_2)|K_g(R, T_2)|^2$. (d) The norm square of the nuclear wave packet from the $2p\sigma_u$ state entering the doubly ionized state for different second jump times T_2 , i.e. $\Gamma_u(R, T_2)|K_u(R, T_2)|^2$.

Once the first jump occurs, the first ionization event takes place and the nuclear wave packet starts to evolve in the H_2^+ system. As one can see from Fig. 3.1(b), the initial wave packets for evolution in H_2^+ are different for different first jump times. This means that the evolution of the nuclear wave packet in H_2^+ is determined by its corresponding first jump time T_1 . For example, in Fig. 3.2, we present some results for the case where the first jump takes place at $T_1 = -13.4$ fs [marked by the red asterisk in Fig. 3.1(d)]. Similar to Fig. 3.1(a), Figs. 3.2(a) and (b) show the evolution of the norm squares of the nuclear wave packets along the $1s\sigma_g$ and $2p\sigma_u$ curves in H_2^+ . Compared with Fig. 3.1(a), significant nuclear dynamics along the $1s\sigma_g$ curve in H_2^+ is induced, because the starting position $R \sim 1.5$ of the initial nuclear wave packet deviates from the equilibrium position ($R = 2$) of the $1s\sigma_g$ curve. [Fig. 3.2(a)]. The wave packet evolving along the $2p\sigma_u$ curve is much weaker, which mainly comes from the dipole coupling between the $1s\sigma_g$ and $2p\sigma_u$

states. For example, three-photon resonance between the $1s\sigma_g$ and $2p\sigma_u$ states results in a relatively large amount of population around $R = 4$ in Fig. 3.2(b). Although there is a small probability for the nuclear wave packet along the $1s\sigma_g$ curve to reach large internuclear separations with $R > 5$ [see the zoomed inset in Fig. 3.2(a)], the dissociation behavior of the nuclear wave packet along the $2p\sigma_u$ curve is more strengthened.

Similar to Fig. 3.1(b), Figs. 3.1(c) and (d) show the amount of the population in the $1s\sigma_g$ and $2p\sigma_u$ states entering the doubly ionized state, respectively. The ionization rate from the $1s\sigma_g$ state $\Gamma_g(R, t)$ is several orders of magnitude smaller than that from the $2p\sigma_u$ state $\Gamma_u(R, t)$ at this peak intensity. Thus, the population entering H_2^{++} from the $1s\sigma_g$ state is much smaller than that from the $2p\sigma_u$ state, as we can see from Figs. 3.2 (c) and (d). Compared with Fig. 3.2(b), there are two enhancements in the distribution around $R = 7$ and $R = 11$ in Fig. 3.2(d), originating from charge-resonance enhance ionization (CREI).

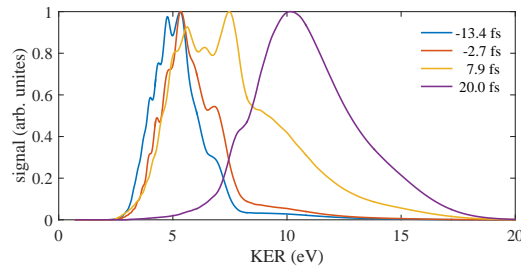


Figure 3.3: The renormalized nuclear KER spectra for the first jump occurring at -13.4 fs, -2.7 fs, 7.9 fs and 20 fs. The laser parameters are same as Figs. 3.1 and 3.2.

Each wave packet at a given second jump time T_2 in Figs. 3.2(a) and (b) results in a KER spectrum, which can be calculated according to Eq. (2.50). Thus, one can obtain the nuclear KER spectrum for $T_1 = -13.4$ fs by summing over the individual KER spectra for different second jump times, as shown in Fig. 3.3. Similarly, one can obtain the nuclear KER spectra for the other first jump times. For comparison, we also show the KER spectra in Fig. 3.3 for the first jump occurring at -2.7 fs, 7.9 fs and 20 fs [marked by the three blue asterisks in Fig. 3.1(d)]. From Fig. 3.3, we can clearly see that early first jumps contribute to small kinetic energies, while late first jumps to large kinetic energies. This is because there is longer time for the nuclei to move to larger internuclear separations with smaller Coulomb repulsion energies at earlier first jumps.

Summing over all the KER spectra for different first jump times, one can obtain the total nuclear KER spectrum after double ionization of H_2 exposed to intense laser pulses. In Fig. 3.4(a), the nuclear KER spectra for several peak intensities ranging from 4×10^{13} W/cm² to 8×10^{13} W/cm² are shown. Increasing the peak intensity of the laser pulse results in the nuclear KER spectrum moving towards lower kinetic energies, even though the positions of the individual peaks in different spectra are quite similar. This can be explained by the fact that increasing the peak intensity is equivalent to increasing the effective duration of the applied laser pulse, thus resulting in increasing the probability for the nuclei moving to

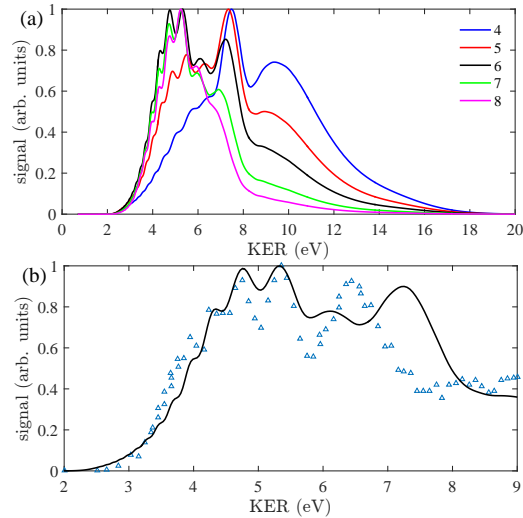


Figure 3.4: (a) The renormalized nuclear KER spectra after double ionization of H₂ interacting with laser pulses of 800 nm, 40 fs and peak intensities ranging from 4×10^{13} W/cm² to 8×10^{13} W/cm². (b) The nuclear KER spectrum after focal volume averaging with a center peak intensity of 7×10^{13} W/cm², together with the nuclear spectrum with a center peak intensity of 10×10^{13} W/cm² taken from Ref. [32]. The laser pulses considered in our simulation has the same wavelength (800 nm) and duration (40 fs) as that applied in the experiment in Ref. [32].

larger internuclear separations. To achieve better agreement with the experimental results, we should conduct focal volume averaging [33], because the dimension of the molecular sample is usually larger than that of the focal beam waist. As a result, in Fig. 3.4(b), we also plot the nuclear KER spectrum with focal volume averaging, together with the experimental result taken from Ref. [32]. In that experiment, the applied laser pulse has the same pulse duration and wavelength as that in our simulation, i.e., 40 fs and 800 nm. Instead of using the experimental center peak intensity of 10×10^{13} W/cm², a center peak intensity of 7×10^{13} W/cm² is applied in our simulation. Our simulation can reproduce several low-energy peaks in the experimental spectrum. However, the peak around 6.5 eV in the experiment is not well reproduced. This disagreement motivates us to include a few excited states in our model, as discussed in Chapter 4. The origin of the peaks in our calculated nuclear KER spectra would be discussed in detail in next section.

3.2 Nuclear KER spectra for single laser pulses

In this section, the influences of laser parameters, such as central wavelength and pulse duration, on the KER spectra are considered. To our knowledge, the behavior of the nuclear KER spectra with increasing wavelengths from the near-IR region to the mid-IR region has not been studied systematically. The large wavelengths of the intense IR laser

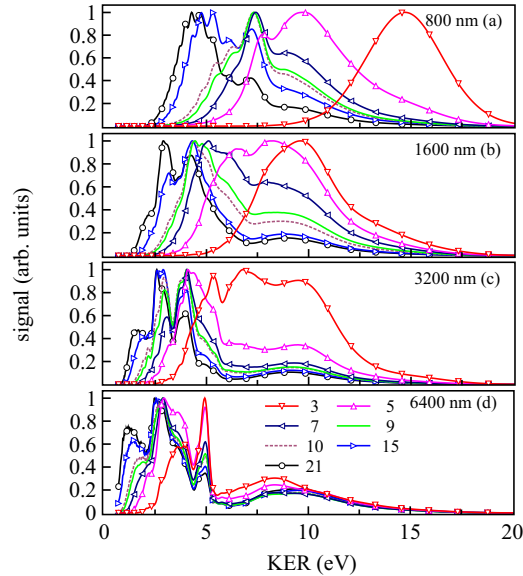


Figure 3.5: (a)-(d) Renormalized nuclear KER spectra after double ionization of H_2 interacting with laser pulses with different wavelengths ranging from 800 nm to 6400 nm and with different FWHM pulse durations ranging from 3 to 21 optical cycles, taken from Ref. [1]. All the pulses have the same peak intensity of $6 \times 10^{13} \text{ W/cm}^2$.

pulses make the ionization dynamics of molecules enter the tunneling regime. As we will show later in this section, studying the peaks in the KER spectra at mid-IR wavelengths by carrying out a trajectory analysis can help to obtain knowledge of the nuclear motion.

The nuclear KER spectra for laser pulses with central wavelengths ranging from 800 nm to 6400 nm and with pulse durations ranging from 3 to 21 optical cycles are given in Fig. 3.5. The peak intensity of all the applied laser pulses is $6 \times 10^{13} \text{ W/cm}^2$. As we can see from Fig. 3.5, for a fixed wavelength, the nuclear KER spectra move towards lower kinetic energies when increasing the number of optical cycles from 3 to 21. Similarly, for a fixed number of optical cycles, the nuclear KER spectra are also moving towards lower kinetic energies when increasing the central wavelength from 800 nm to 6400 nm. Thus, it is reasonable to draw the conclusion that the pulse duration, which is proportional to the product of the wavelength and the number of optical cycles of a laser pulse, determines how the nuclear KER spectra behaves as a whole for a given peak intensity.

We notice that the broad peaks $\sim 9 \text{ eV}$ appear in nearly all the plots in Fig. 3.5, which means that these peaks are almost independent of laser wavelength. Besides, several peaks in the spectra are more or less at similar positions, e.g., when the number of optical cycles is greater than 7 for the 800 nm case, as shown in Fig. 3.5(a). Similar feature can be observed for the other three cases, though they have different individual peak positions, which means that these peak positions are closely dependent on the laser wavelength.

The final proton picks kinetic energy from two parts, one is the dissociative kinetic energy in H_2^+ and the other is the Coulomb repulsion energy in H_2^{++} . The fact that the peaks ~ 9 eV nearly do not depend on the laser wavelength means that these peaks come from the ionization events before the nuclear wave packets evolving along the $1s\sigma_g$ curve reach the positions of the resonant dipole coupling between the $1s\sigma_g$ and $2p\sigma_u$ in H_2^+ . Thus these peaks are mainly from large ionization when the nuclear wave packets nearly stop at the outer turning point ($R \sim 3$) of the $1s\sigma_g$ curve, because the initial nuclear wave packets in H_2^+ start at $R \sim 1.5$. Several other wavelength-dependent peaks appearing in the spectra can be ascribed to four ionization pathways, i.e., large ionization at positions of the one- and three-photon resonances between the $1s\sigma_g$ and $2p\sigma_u$ states in H_2^+ , and larger ionization at the two CREI positions after the one- and three-photon resonances between the $1s\sigma_g$ and $2p\sigma_u$ states in H_2^+ . For example, for the 800 nm case, the peaks around 7 eV are mainly from large ionization at the position of the three-photon resonance between the $1s\sigma_g$ and $2p\sigma_u$ states in H_2^+ , and the peaks around 4 eV are mainly from large ionization at the CREI position of $R = 7$.

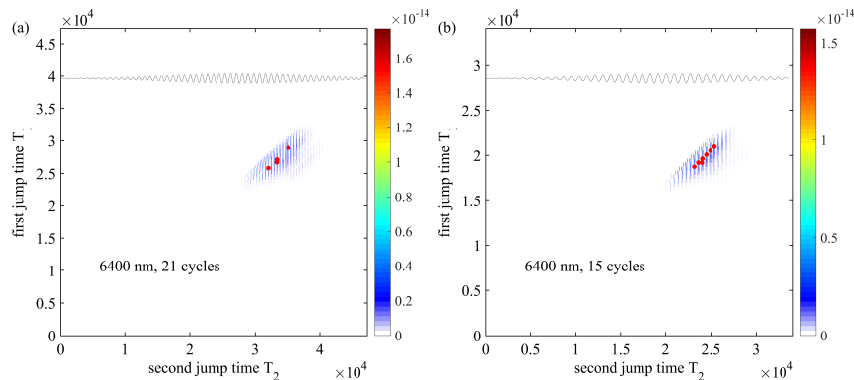


Figure 3.6: (a) Contributions from different trajectories to the low-energy peak around 1.2 eV in Fig. 3.5(d) when interacting with a pulse with 21 optical cycles at 6400 nm, taken from Ref. [1]. (b) Contributions from different trajectories to the low-energy peak around 1.5 eV in Fig. 3.5(d) when interacting with a pulse with 15 optical cycles at 6400 nm. The red dots in (a) and (b) mark the trajectories which give the largest contributions. The laser pulses are indicated by the grey lines and the parameters are as in Fig. 3.5(d).

In the above mentioned four ionization pathways, ionization events taking place at the CREI position of $R = 11$ would result in protons with the smallest kinetic energies with the Coulomb repulsion energy around $\frac{1}{11} = 2.47$ eV. The low-energy peaks smaller than 2 eV in Figs. 3.5(c) and (d) are from another ionization pathway, i.e., large ionization in the dissociation limit at large internuclear separations. These peaks come to birth when the pulse duration is large, e.g., 10 or more optical cycles for 3200 nm and 5 or more optical cycles for 6400 nm. We conduct a trajectory analysis of the two low-energy peaks in Fig. 3.5(d), i.e., around 1.5 eV for 15 optical cycles and around 1.2 eV for 21 optical cycles. In Fig. 3.6, contributions from different trajectories to these two low-energy peaks are

shown. The trajectories which give the largest contributions are marked by the red dots. The time difference between the first jump time and the second jump time is actually the evolution time of the nuclear wave packet in H_2^+ . We can see from Fig. 3.6, the evolution time for the peak around 1.2 eV is about 6000 (~ 150 fs), and the evolution time for the peak around 1.5 eV is about 4000 (~ 100 fs). These times are large enough for the nuclear wave packet to reach large internuclear separations ($R > 20$).

3.3 Nuclear KER spectra in a pump-probe scheme

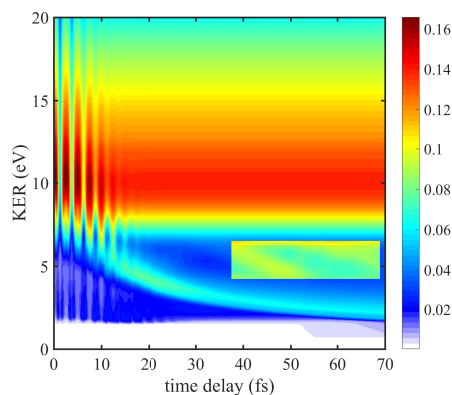


Figure 3.7: Nuclear KER distributions as a function of time delay between pump and probe pulses, a slightly modified version of Fig. 5(a) in Ref. [1]. The peak intensity of the pump (probe) pulse is 4×10^{14} W/cm² (6×10^{13} W/cm²). The two pulses have the same wavelength (750 nm) and the same duration (3 optical cycles). The data are plotted to the power of 0.2 in order to gain a larger visibility of the structures and after that the signal in the insert was multiplied by a factor of 3.

When molecules interact with two or more laser pulses, dynamics of the nuclei as well as dynamics of the photoelectrons can be studied as a function of the time delay between the pulses. In Fig. 3.7, we plot the simulated KER distributions as a function of time delay between pump and probe laser pulses with their polarization axes parallel to the molecular axis. In order to test the performance of our approach, the parameters of the two laser pulses are chosen according to Ref. [34]: The central wavelength and the FWHM duration of the two pulses are 750 nm and 3 optical cycles, respectively. The pump laser has a peak intensity of 4×10^{14} W/cm² while the probe has a peak intensity of 6×10^{13} W/cm². We find a good agreement between Fig. 3.7 and the experimental results of Ref. [34]. In particular, the high-energy branch around 10 eV and the energy-decreasing branch from 6 eV to 2 eV for increasing time delay are reproduced.

In Fig. 3.7, the channel with KER around 10 eV mainly comes from double ionization of H_2 by the more intense pump pulse. This channel shows no delay dependence when the delay is larger than 20 fs. However, for delays smaller than 20 fs, oscillation of the

KER distributions with a period of one optical cycle is observed. This oscillation is a signature of constructive and destructive interference between the two pulses when the two pulses overlap in time. The channel with KER in the 2-6 eV range has a strong delay dependence and is due to the ionization of H_2^+ by the relatively weak probe pulse. The main energy-decreasing branch from 6 eV to 2 eV for increasing delay is a result of the nuclear wave packet moving along the $2p\sigma_u$ potential energy curve in H_2^+ .

In addition, there are two much weaker energy-decreasing branches. A zoom of part of the branches is shown in the insert to the right of Fig. 3.7. These branches can be shown to result from the oscillatory movement of the nuclear wave packet along the $1s\sigma_g$ potential energy curve in H_2^+ : The duration between the first dominant decreasing branch starting at a time delay around 15 fs and the second branch highlighted in the insert is around 20-25 fs corresponding to a full oscillatory motion in the $1s\sigma_g$ curve.

4 Dissociative double ionization of H_2 exposed to intense laser pulses under the influence of a doubly-excited state

In this Chapter, compared with the previous chapter, the influence of a doubly-excited state as well as the process of autoionization on the nuclear KER spectra is considered. Several preliminary results are presented below. Doubly-excited states are highly correlated Rydberg states converging to different ionization thresholds. In molecules, these states are metastable and can either dissociate into two neutral fragments, or can decay into the electronic continuum before dissociating into neutrals by ejecting an electron. The latter process is called autoionization, where one electron is freed and the other remains bound resulting from the energy exchange between the two bound electrons through electron-electron correlation.

It has been shown experimentally by several groups [35, 36] that autoionization can lead to symmetry breaking in the photoelectron momentum spectrum, .i.e., electron localization, as a result of the interaction between direct ionization pathways and the autoionization pathways. The influence of the autoionizing states on the nuclear KER spectra is, however, not studied thoroughly.

In Chapter 2, we discuss in detail how to apply the MCWP approach to dissociative double ionization of H_2 . To include a doubly excited state successfully into our model, several properties of the new state (similarly, short for d) are required, e.g., the Born-Oppenheimer field-free electronic potential energy curve $E_d(R)$, the R -dependent autoionization rates $\Gamma_d(R)$, as well as the dipole moment function between the ground state and this doubly-excited state $D_{hd}(R)$.

The doubly excited state we are considering now is in the same Hilbert space with the ground state, thus the evolution of the radial nuclear wave packet in H_2 is now expressed

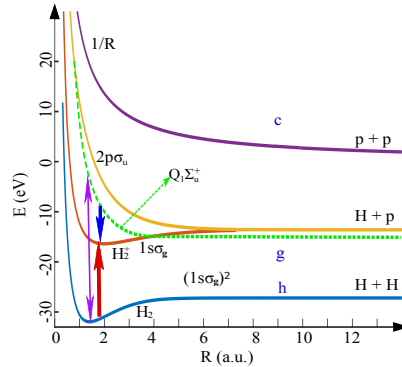


Figure 4.1: Sketch of the potential energy curve of the doubly-excited state of $Q_1\Sigma_u^+$ (green dashed line) and the associated processes. The pink arrow means the dipole coupling between the doubly-excited state and the ground state in H_2 . The blue (red) arrow represents the process of autoionization (photoionization).

as

$$i \begin{bmatrix} \dot{K}_h \\ \dot{K}_d \end{bmatrix} = \begin{bmatrix} E_h(R) - i\frac{\Gamma_h(R,t)}{2} & D_{hd}(R)F(t) \\ D_{dh}(R)F(t) & E_d(R) - i\frac{\Gamma_d(R)}{2} \end{bmatrix} \times \begin{bmatrix} K_h \\ K_d \end{bmatrix}, \quad (4.1)$$

while the evolution of the nuclear wave packet in H_2^+ and H_2^{++} is the same as before. $\Gamma_d(R)$ is the autoionization rate to the $1s\sigma_g$ state in H_2^+ . Equation (4.1) also implies that just as the second jump, the first jump here can take place either at the h state or at the d state with a weighed probability.

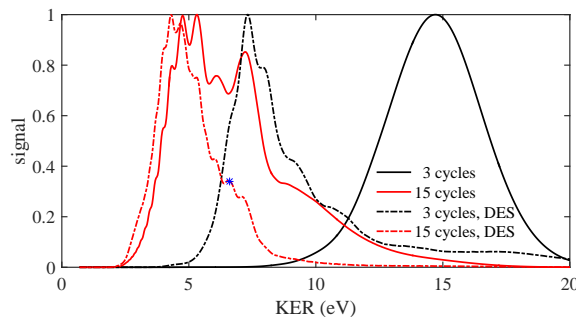


Figure 4.2: Nuclear KER spectra obtained with and without the influence of the doubly-excited state of $Q_1\Sigma_u^+$ for H_2 interacting with laser pulses at 800 nm with durations of 3 and 15 optical cycles. The solid (dash) lines represent KER spectra without (with) considering the doubly excited state. All the applied laser pulses have a peak intensity of $6 \times 10^{13} \text{W/cm}^2$

We consider the influence of the lowest doubly excited state of $Q_1\Sigma_u^+$, the properties of which could be found in some literatures [37, 38, 39]. The respective nuclear KER spectra for H_2 interacting with laser pulses with 3 and 15 optical cycles at 800 nm are shown is

Fig. 4.2. We can see that, for the case of 3 optical cycles, the two KER spectra are dramatically different, with the spectrum under the influence of the doubly excited state moving to much lower kinetic energies. The influence of the doubly excited states will be considered carefully in the future.

5 Summary and Outlook

In this report, how to apply the MCWP approach to simulate dissociative double ionization of H_2 exposed to intense femtosecond laser pulses is discussed in detail. The calculated nuclear KER spectra of protons after double ionization for different intensities and wavelengths are presented and discussed. Our main findings are (1) there is a trend towards lower kinetic energies when increasing the peak intensity from $4 \times 10^{13} \text{ W/cm}^2$ to $8 \times 10^{13} \text{ W/cm}^2$; (2) there is a trend towards lower kinetic energies when increasing the central wavelength from near-IR regime to mid-IR regime; (3) the peaks in the nuclear KER spectra can reflect CREI as well as the one- and three-photon resonances between the $1s\sigma_g$ and $2p\sigma_u$ states in H_2^+ ; (4) a trajectory analysis can help to find the origin of the peaks in the nuclear KER spectrum.

In addition, the preliminary results of the nuclear KER spectra under the influence of the doubly-excited state in Chapter 4 show that the inclusion of a doubly-excited state may significantly affect the nuclear KER spectrum, especially for the case of short laser pulses.

There are many open questions for the processes related to excited states. In the future, we will keep on studying the influences of the singly- and doubly-excited states in H_2 and other excited states in H_2^+ on the nuclear KER spectra when interacting with femtosecond laser pulses. The processes of photoionization from excited states and autoionization from doubly-excited states both would be involved in our calculation. In fact, it is not an easy task to get the ionization rates from different states. Apart from femtosecond laser pulses, attosecond XUV pulses can be further introduced into our system as a pump to efficiently populate several doubly-excited states and thus induces autoionization. Furthermore, we can also get some insight into the motion of photoelectrons by doing a classical description of the photoelectrons.

As part of my PhD program, a short stay in MADRID next year is planned.

References

- [1] Q. L. Jing and L. B. Madsen. Laser-induced dissociative ionization of H_2 from the near-infrared to the mid-infrared regime, in press. *Phys. Rev. A*, 2016.
- [2] T. H. Maiman. Stimulated optical radiation in ruby. *SPIE milestone series*, (173):61–61, 2002.

-
- [3] J. Weiner and P.-T. Ho. *Light-matter interaction, Fundamentals and applications*, volume 1. John Wiley & Sons, 2008.
- [4] M. Uiberacker, T. Uphues, M. Schultze, A. J. Verhoef, V. Yakovlev, M. F. Kling, J. Rauschenberger, N. M. Kabachnik, H. Schröder, M. Lezius, et al. Attosecond real-time observation of electron tunnelling in atoms. *Nature*, 446(7136):627–632, 2007.
- [5] M. F. Kling, C. Siedschlag, A. J. Verhoef, J. I. Khan, M. Schultze, T. Uphues, Y. Ni, M. Uiberacker, M. Drescher, F. Krausz, et al. Control of electron localization in molecular dissociation. *Science*, 312(5771):246–248, 2006.
- [6] L. Childress, M. V. G. Dutt, J. M. Taylor, A. S. Zibrov, F. Jelezko, J. Wrachtrup, P. R. Hemmer, and M. D. Lukin. Coherent dynamics of coupled electron and nuclear spin qubits in diamond. *Science*, 314(5797):281–285, 2006.
- [7] U. Keller, D. A. B. Miller, G. D. Boyd, T. H. Chiu, J. F. Ferguson, and M. T. Asom. Solid-state low-loss intracavity saturable absorber for nd:y:lyf lasers: an antiresonant semiconductor fabry-perot saturable absorber. *Opt. Lett.*, 17(7):505–507, 1992.
- [8] U. Keller, K. J. Weingarten, F. X. Kartner, D. Kopf, B. Braun, I. D. Jung, R. Fluck, C. Honninger, N. Matuschek, and J. Aus der Au. Semiconductor saturable absorber mirrors (SESAM's) for femtosecond to nanosecond pulse generation in solid-state lasers. *IEEE Journal of Selected Topics in Quantum Electronics*, 2(3):435–453, 1996.
- [9] D. J. Jones, S. A. Diddams, J. K. Ranka, A. Stentz, R. S. Windeler, J. L. Hall, and S. T. Cundiff. Carrier-envelope phase control of femtosecond mode-locked lasers and direct optical frequency synthesis. *Science*, 288(5466):635–639, 2000.
- [10] P. M. Paul, E. S. Toma, P. Breger, G. Mullot, F. Augé, Ph. Balcou, H. G. Muller, and P. Agostini. Observation of a train of attosecond pulses from high harmonic generation. *Science*, 292(5522):1689–1692, 2001.
- [11] M. Hentschel, R. Kienberger, C. Spielmann, G. A. Reider, N. Milosevic, T. Brabec, P. Corkum, U. Heinzmann, M. Drescher, and F. Krausz. Attosecond metrology. *Nature*, 414(6863):509–513, 2001.
- [12] P. Tzallas, E. Skantzakis, C. Kalpouzos, E. P. Benis, G. D. Tsakiris, and D. Charalambidis. Generation of intense continuum extreme-ultraviolet radiation by many-cycle laser fields. *Nat. phys.*, 3(12):846–850, 2007.
- [13] T. Pfeifer, L. Gallmann, M. J. Abel, P. M. Nagel, D. M. Neumark, and S. R. Leone. Heterodyne mixing of laser fields for temporal gating of high-order harmonic generation. *Phys. Rev. Lett.*, 97:163901, 2006.
- [14] G. Sansone, E. Benedetti, F. Calegari, C. Vozzi, L. Avaldi, R. Flammini, L. Poletto, P. Villoresi, C. Altucci, R. Velotta, S. Stagira, S. De Silvestri, and M. Nisoli. Isolated single-cycle attosecond pulses. *Science*, 314(5798):443–446, 2006.

-
- [15] F. Ferrari, F. Calegari, M. Lucchini, C. Vozzi, S. Stagira, G. Sansone, and M. Nisoli. High-energy isolated attosecond pulses generated by above-saturation few-cycle fields. *Nat. Photonics*, 4(12):875–879, 2010.
- [16] K. Codling and J. Frasinski, L. Dissociative ionization of small molecules in intense laser fields. *J. Phys. B: At. Mol. Opt. Phys.*, 26(5):783, 1993.
- [17] R. Dörner, V. Mergel, O. Jagutzki, L. Spielberger, J. Ullrich, R. Moshhammer, and H. Schmidt-Böcking. Cold target recoil ion momentum spectroscopy: a ‘momentum microscope’ to view atomic collision dynamics. *Phys. Rep.*, 330(2):95–192, 2000.
- [18] A. T. J. B. Eppink and D. H. Parker. Velocity map imaging of ions and electrons using electrostatic lenses: Application in photoelectron and photofragment ion imaging of molecular oxygen. *Rev. Sci. Instrum.*, 68(9):3477–3484, 1997.
- [19] H. G. Muller. Reconstruction of attosecond harmonic beating by interference of two-photon transitions. *Appl. Phys. B*, 74(1):s17–s21, 2002.
- [20] J. Itatani, F. Quéré, G. L. Yudin, M. Yu. Ivanov, F. Krausz, and P. B. Corkum. Attosecond streak camera. *Phys. Rev. Lett.*, 88:173903, 2002.
- [21] A. Palacios, J. L. Sanz-Vicario, and F. Martín. Theoretical methods for attosecond electron and nuclear dynamics: applications to the H₂ molecule. *J. Phys. B: At., Mol. Opt. Phys.*, 48(24):242001, 2015.
- [22] T. Popmintchev, M.-C. Chen, D. Popmintchev, P. Arpin, S. Brown, S. Ališauskas, G. Andriukaitis, T. Balčiunas, O. D. Mücke, A. Pugzlys, A. Baltuška, B. Shim, S. E. Schrauth, A. Gaeta, C. Hernández-García, L. Plaja, A. Becker, A. Jaron-Becker, M. M. Murnane, and H. C. Kapteyn. Bright coherent ultrahigh harmonics in the keV X-ray regime from mid-infrared femtosecond lasers. *Science*, 336(6086):1287–1291, 2012.
- [23] J. Caillat, J. Zanghellini, M. Kitzler, O. Koch, W. Kreuzer, and A. Scrinzi. Correlated multielectron systems in strong laser fields: A multiconfiguration time-dependent Hartree-Fock approach. *Phys. Rev. A*, 71:012712, 2005.
- [24] J. L. Sanz-Vicario, H. Bachau, and F. Martín. Time-dependent theoretical description of molecular autoionization produced by femtosecond xuv laser pulses. *Phys. Rev. A*, 73:033410, 2006.
- [25] F. Calegari, D. Ayuso, A. Trabattoni, L. Belshaw, S. De Camillis, S. Anumula, F. Frassetto, L. Poletto, A. Palacios, P. Decleva, J. B. Greenwood, F. Martín, and M. Nisoli. Ultrafast electron dynamics in phenylalanine initiated by attosecond pulses. *Science*, 346(6207):336–339, 2014.
- [26] H. A. Leth. *Dissociative ionization - a study using the Monte Carlo Wave Packet Approach*. PhD dissertation, Aarhus University, Department of Physics and Astronomy, 2011.

-
- [27] H. Kono, Y. Sato, Y. Fujimura, and I. Kawata. Identification of the doorway states to ionization of molecules in intense laser fields. *Laser Phys.*, 13(6):883–888, 2003.
- [28] M. D. Feit, J. A. Fleck, and A Steiger. Solution of the schrödinger equation by a spectral method. *J. Comput. Phys.*, 47(3):412 – 433, 1982.
- [29] Oleg I. Tolstikhin, Toru Morishita, and Lars Bojer Madsen. Theory of tunneling ionization of molecules: Weak-field asymptotics including dipole effects. *Phys. Rev. A*, 84:053423, 2011.
- [30] J. T. Lin and T. F. Jiang. Photodissociation of H_2^+ in intense chirped laser fields. *Phys. Rev. A*, 63:013408, 2000.
- [31] Martin Plummer and James F McCann. Field-ionization rates of the hydrogen molecular ion. *J. Phys. B: At., Mol. Opt. Phys.*, 29(20):4625, 1996.
- [32] A. Staudte, D. Pavičić, S. Chelkowski, D. Zeidler, M. Meckel, H. Niikura, M. Schöffler, S. Schössler, B. Ulrich, P. P. Rajeev, Th. Weber, T. Jahnke, D. M. Villeneuve, A. D. Bandrauk, C. L. Cocke, P. B. Corkum, and R. Dörner. Attosecond strobing of two-surface population dynamics in dissociating H_2^+ . *Phys. Rev. Lett.*, 98:073003, 2007.
- [33] P. Q. Wang, A. M. Sayler, K. D. Carnes, B. D. Esry, and I. Ben-Itzhak. Disentangling the volume effect through intensity-difference spectra: application to laser-induced dissociation of H_2^+ . *Opt. Lett.*, 30(6):664–666, 2005.
- [34] H. Xu, F. He, D. Kielpinski, R. T. Sang, and I. V. Litvinyuk. Experimental observation of the elusive double-peak structure in R-dependent strong-field ionization rate of H_2^+ . *Sci. Rep.*, 5:13527, 2015.
- [35] G. Sansone, F. Kelkensberg, J. F. Pérez-Torres, F. Morales, M. F. Kling, W. Siu, O. Ghafur, P. Johnsson, M. Swoboda, E. Benedetti, et al. Electron localization following attosecond molecular photoionization. *Nature*, 465(7299):763–766, 2010.
- [36] A. Fischer, A. Sperl, P. Cörlin, M. Schönwald, H. Rietz, A. Palacios, A. González-Castrillo, F. Martín, T. Pfeifer, J. Ullrich, et al. Electron localization involving doubly excited states in broadband extreme ultraviolet ionization of H_2 . *Phys. Rev. Lett.*, 110(21):213002, 2013.
- [37] S. L. Guberman. The doubly excited autoionizing states of H_2 . *J. Chem. Phys.*, 78(3):1404–1413, 1983.
- [38] J. I. Borges and C. E. Bielschowsky. Doubly excited states of molecular hydrogen: theoretical absorption and photodissociation cross sections. *J. Phys. B: At., Mol. and Opt. Phys.*, 33(9):1713, 2000.
- [39] K. Kirby, S Guberman, and A Dalgarno. Resonant dissociative photoionization of H_2 . *J. Chem. Phys.*, 70(10):4635–4639, 1979.